The sensitizing effects of NO_2 and NO on methane low temperature oxidation in a jet stirred reactor

Y. Song [a], L. Marrodán [b], N. Vin [a], O. Herbinet [a, *], E. Assaf [c], C. Fittschen [c], A. Stagni [d], T. Faravelli [d], M.U. Alzueta [b], F. Battin-Leclerc [a]

[a] Laboratoire Réactions et Génie des Procédés, CNRS-Université de Lorraine, 1 rue Grandville, 54000 Nancy, France. [*]olivier.herbinet@univ-lorraine.fr

[b] Aragón Institute of Engineering Research (I3A), Department of Chemical and Environmental Engineering, University of Zaragoza, Mariano Esquillor s/n, 50018 Zaragoza, Spain.

[c] Université Lille, CNRS, UMR 8522- PC2A-PhysicoChimie des Processus de Combustion et de l'Atmosphère, F59000 Lille, France.

[d] Department of Chemistry, Materials and Chemical Engineering "G. Natta ", Politecnico di Milano, P.zza Leonardo da Vinci 32, 20133 Milano, Italy.

SUPPLEMENTAL INFORMATION

Table of content

Fig.S12. The simulation work of the evolution profiles of methane as a function of time for the oxidation of methane doped with NO_2 at 1100 K under stoichiometric condition. **(Oscillations)**

4) Evolution with temperature of mole fractions of the different species according to model calculations with POLIMI mechanism.

A) For the addition of 400 ppm of NO_2 and Φ=2.

Fig.S13. Evolution with temperature of mole fractions for the carbon compound species, H_2O and H_2 predicted by the POLIMI mechanism for the addition of 400 ppm of NO_2 and Φ=2.

Fig.S14. Evolution with temperature of mole fractions for the nitrogen containing species predicted by the POLIMI mechanism for the addition of 400 ppm of NO_2 and Φ=2

B) For the addition of 400 ppm of NO_2 and Φ=0.5.

Fig.S15. Evolution with temperature of mole fractions for the carbon compound species, H_2O and H_2 predicted by the POLIMI mechanism for the addition of 400 ppm of NO_2 and Φ=0.5.

Fig.S16. Evolution with temperature of mole fractions for the nitrogen containing species predicted by the POLIMI mechanism for the addition of 400 ppm of NO_2 and Φ=0.5.

C) For the addition of 500 ppm of NO and Φ=2.

Fig.S17. Evolution with temperature of mole fractions for the carbon compound species, H_2O and H_2 predicted by the POLIMI mechanism for the addition of 500 ppm of NO and Φ=2.

Fig.S18. Evolution with temperature of mole fractions for the nitrogen containing species predicted by the POLIMI mechanism for the addition of 500 ppm of NO and Φ=2.

D) For the addition of 500 ppm of NO and Φ=0.5.

Fig.S19. Evolution with temperature of mole fractions for the carbon compound species, H_2O and H_2 predicted by the POLIMI mechanism for the addition of 500 ppm of NO and Φ=0.5.

Fig.S20. Evolution with temperature of mole fractions for the nitrogen containing species predicted by the POLIMI mechanism for the addition of 500 ppm of NO and Φ=0.5.

5) The performance of literature models against the experimental data

Fig.S21. The performance of different models against the experiment data (mole fraction of methane) with neat methane oxidation under stoichiometric conditions.

Fig.S22. The performance of different models against the experiment data (mole fraction of methane) with the oxidation of methane doped with NO_2 under stoichiometric conditions.

Fig.S23. The performance of different models against the experiment data (mole fraction of methane) with the oxidation of methane doped with NO under stoichiometric conditions.

Fig.S24. The performance of different models against the experiment data (mole fraction of NO_x) with the oxidation of methane doped with NO_2 under stoichiometric conditions.

Fig.S25. The performance of different models against the experiment data (mole fraction of NO_x) with the oxidation of methane doped with NO under stoichiometric conditions.

6) Comparison of FTIR spectra for HCN with the spectra obtained during the oxidation of methane doped with NO.

Fig.S26. Comparison of the FTIR spectra for HCN [7] with the spectra obtained during the oxidation of methane doped with NO (500 ppm NO, 1200 K and Φ=2).

7) Comparison of FTIR spectra for CH_3NO_2 with the spectra obtained during the oxidation of methane doped with NO_2.

Fig.S27. Comparison of the FTIR spectra obtained for CH_3NO_2 with the spectra obtained during the oxidation of methane doped with NO_2 (400 ppm NO_2, 900 K and Φ=0.5).

8) Comparison of cw-CRDS spectra for HONO with the spectra obtained during the oxidation of methane doped with NO_2.

Fig.S28. Comparison of the HONO cw-CRDS spectra with the spectra obtained during the oxidation of CH_4 doped with 400 ppm NO_2, at 850 K and Φ=0.5. Red line: absorption spectrum measured in this work (left axis), black line: HONO spectrum from Jain et al. [4], green line: CH_2O absorption spectrum from Ruth et al. [5], multiplied by 12, blue bars: CH_4 line strengths from Liu et al. [6], multiplied by 10^4.

9) Comparisons between the original POLIMI model and POLIMI model with $CH_3+NO_2=CH_2O+NO$ modified against the experimental data under different conditions

Fig.S29. Comparisons between the original POLIMI model and POLIMI model with $CH_3+NO_2=CH_2O+NO$ modified against the experimental results from the oxidation of methane doped with NO_2 under stoichiometric conditions

Fig.S30. Comparisons between the original POLIMI model and POLIMI model with $CH_3+NO_2=CH_2O+NO$ modified against the experimental results from the oxidation of methane doped with NO under stoichiometric conditions

1) Additional description of the experimental setup

A) Jet-stirred reactor (JSR)

The jet-stirred reactor (JSR) used in this study is spherical with a volume of about 85 cm^3. It is preceded by an annular preheater in which the reacting mixture is progressively heated up to the reaction temperature. Then the reacting mixture enters the reactor trough four injectors with noozles which creates high turbulence and homogenous mixing. The annular preheater and the reactor are made of fused silica. The heating is providing through Thermocoax resistances rolled around the preheater and the reactor. The reaction temperature is measured with a type K thermocouple located in a glass finger (the intraannular part of the preheater) at the center of the spherical reactor. Mass flow controllers (Bronkhorst) are used to control the volumetric flow rates of the reactants (CH_4, O_2, NO and NO_2) and the inert gas (Ar). The role of the inert gas is to dilute the reacting mixture in order to slow down the exothermicity of the reactions and to get a better control of the temperature. The pressure inside the reactor (800 Torr=106.7 kPa) is controlled using a manual valve located downstream of the reactor. The gas stream is analyzed online downstream of the reactor with the different diagnostic techniques as followed:

B) Gas chromatography

Two gas chromatographs were used for the online quantification of oxygen and carbon containing species. The first one, a Perichrom PR1250, was used to quantify oxygen. Injection were performed using a six-way gas sampling valve. The column used for the separation was a molecular sieve packed column and the detection was carried out with a thermal conductivity detector. The carrier gas was helium to have a good sensibility for oxygen. The second one, a Perichrom PR2500, was used for the quantification of CO, CO_2 and C_1-C_2 hydrocarbons. Injection were performed using a six-way gas sampling valve. A split of 1:5 was applied in the split injector. The column used for species separation was a PlotQ capillary one. The detection was performed using a flame ionization detector. The gas flow from the column was passed over a heated nickel catalyst for hydrogenation to convert CO and CO_2 to methane before detection. The calibration was performed with calibration bottles provided by Air-Liquide, France. The detection limit is about 10 ppm for the FID, 100 ppm for the TCD and the relative uncertainty is mole fractions is $\pm$5%.

C) NO_x Analysis

A chemiluminescence NO_x analyzer (Model 42i from ThermoFisher Scientific) was used to measure NO and NO_2 mole fractions. The quantitative range is 0-5000 ppm for NO and 0-500 ppm for NO_2 with 0.1 ppm sensitivity, respectively. Two pumps are used for outlet and bypass channels, respectively, enabling the simultaneous measurement of the concentrations of NO and NO_2. Briefly, the detection is based on the reaction of NO with O_3 leading to $NO_2 + O_2 + h\nu$. The light emitted, which is proportional to the concentration of NO, is detected using a photomultiplier tube (PMT). The measurement of NO_2 is indirectly obtained by measuring the total NO_x concentrations and subtracting the concentration of NO. The total NO_x concentrations are determined by converting NO_2 to NO over a heated catalyst prior the reaction chamber where the reaction with ozone takes place. The calibration was made with two calibration bottles provided by Air-Liquide, France, with 5000 ppm NO and 500 ppm NO_2 in argon, respectively. Note that the diluent gas is of importance as it has an effect on the flow rate through the analyzer and that it should be the same as the carrier gas used in experiments. The detection limit is about 1 ppm and the relative uncertainty is NO mole fractions is $\pm$5%, $\pm$10 for NO_2.

D) FTIR analyses

A Fourier Transform InfraRed spectrometer (FTIR) from Thermo Scientific Antaris equipped with a Mercure Cadmium Tellure photoelectric detector was used to analyze HCN and nitromethane. FTIR calibrations were obtained by injecting standards. Nitromethane was provided by Sigma (purity greater than 98.5%) and diluted mixtures were obtained by mixing nitromethane and helium using a Coriolis, a mass flow controller and an evaporation system provided by Bronkhorst, France. HCN was calibrated using a calibration gas bottle provided by Air-Liquide, France (1000 ppm of HCN in nitrogen). Different concentrations were used for calibration by

mixing the diluted HCN with an auxiliary nitrogen flow. The two flows were controlled by mass flow controllers provided by Bronkhorst, France. All FTIR analyses were performed at 373.15 K and 150 Torr. 32 scans were recorded for each analysis. A resolution of 0.5 cm^{-1} was used. The detection limit is about 10 ppm and the relative uncertainty in mole fractions is $\pm$10%,

E) cw-CRDS apparatus

The cw-CRDS cell is composed of a quartz tube with an outer diameter of 8 mm and a length of 80 cm. The total volume of the cell including the sampling probe is estimated to be 40 cm^3. The cell is maintained at ambient temperature through convection and the pressure in the CRDS cavity is kept at approximately 10 Torr. The low pressure is obtained using a rotary vane pump (Alcatel 1015SD with a nominal flow rate of 15 $m^3.h^{-1}$). CRDS analyses were carried out in the near infrared at wavelengths from 6638 – 6643cm^{-1}. The near-infrared beam was provided by a fibred distributed feed-back (DFB) diode laser (Fitel-Furukawa FOL15DCWB-A81-W1509) emitting up to 40 mW, the wavelength can be varied in the range 6640±13 cm^{-1} through changing the current applied to the diode laser. The diode laser emission is directly fibred and passes through a fibred optical isolator and a fibred acousto-optical modulator (AOM, AA Opto-Electronic). The AOM allows the laser beam to be deviated within 350 ns with respect to a trigger signal for a total duration of 1.5 ms. The zero order beam is connected to a fibred optical wave meter (228 Bristol Instruments) for monitoring the wavelength of the laser emission with an accuracy of 0.01 cm^{-1}. The main first order laser beam is coupled into the CRDS optical cavity through a short focal length lens (f = 10 mm) for mode matching so as to excite the fundamental TEM00 mode. Two folding micrometric mirrors allow easy alignment of the beam, as shown in Figure 1. After many round trips, the optical signal transmitted through the cavity is converted into current by an avalanche photodiode (Perkin Elmer C30662E). A home designed amplifierthreshold circuit converts the current signal to an exploitable voltage signal and triggers the AOM to deviate the laser beam (turn off of the first order) as soon as the cavity comes into resonance and the photodiode signal exceeds a user-defined threshold. The photodiode signal is connected to a fast 16 bit analogue acquisition card (PCI-6259, National Instruments) in a PC, which is triggered also by the amplifier-threshold circuit. The acquisition card has an acquisition frequency of 1.25 MHz and thus the ring-down signal is sampled every 800 ns and the data are transferred to PC in real time. The ring-down time is obtained by fitting the exponential decay over a time range of seven lifetimes by a Levenberg-Marquardt exponential fit in LabView. The concentration of a species being formed or consumed during the hydrocarbon oxidation process in a jet-stirred reactor (JSR), can be obtained by measuring the ring-down time of the empty cavity τ_0, i.e., the ring down time before heating the reactor, and the ring down time τ, after turning on the heater:

$$\alpha = [X] \times \sigma = \frac{R}{c}\left(\frac{1}{\tau} - \frac{1}{\tau 0}\right)$$

where σ is the absorption cross section, R is the ratio between the cavity length L, i.e. the distance between the two cavity mirrors to the length LA over which the absorber is present, c is the speed of light. Knowing the absorption cross section, one can extract the concentration [A] of the target molecule. The relative uncertainty is around $\pm$10-15%,

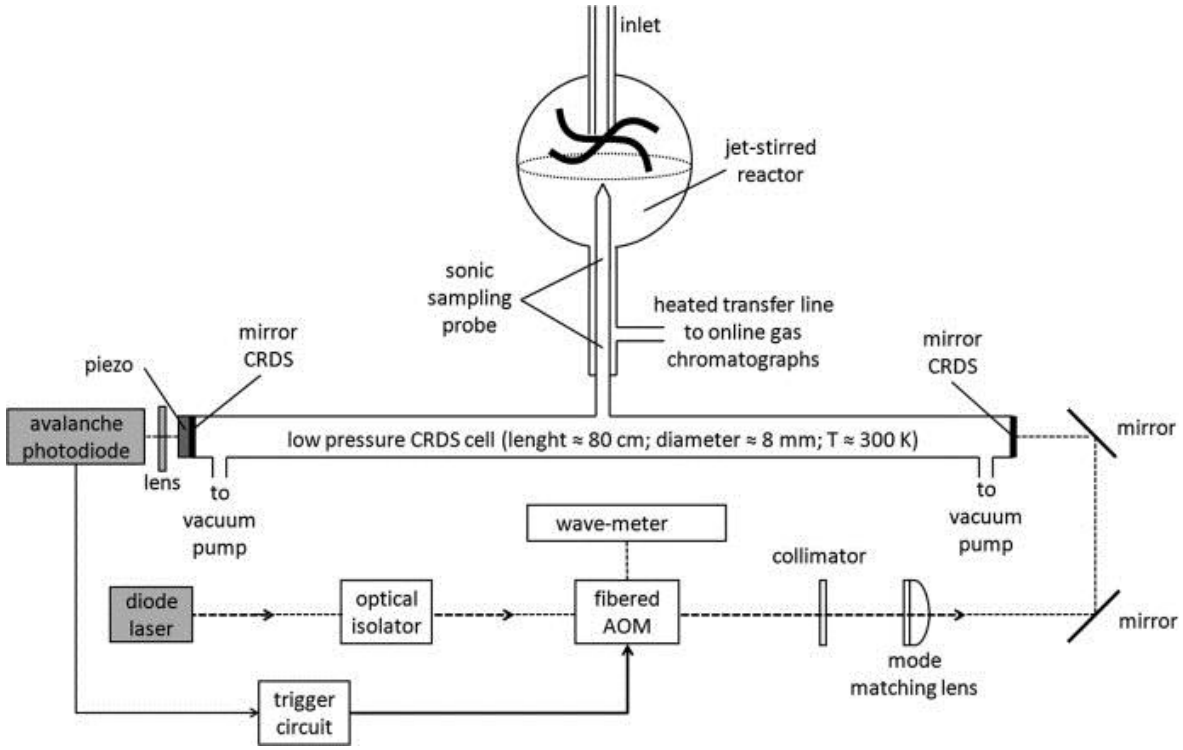

Fig.S1. Schematic view of the JSR and CRDS coupling.

2) Comparison of simulations using the present mechanism (POLIMI mechanism) with literature data.

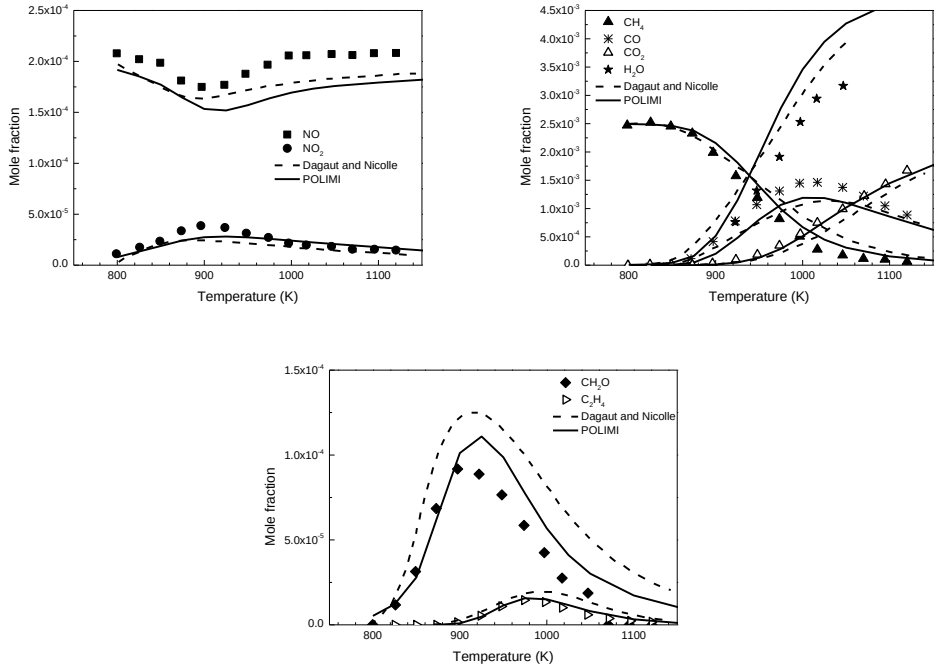

Fig.S2. Comparison of modeling predictions using POLIMI mechanism (solid lines) and experimental (symbols) and modeling predictions (dashed lines) reported by Dagaut and Nicolle [1] for the oxidation of methane and NO in a JSR (1 atm, Φ=0.1, 2500 ppm of CH_4, 50000 ppm of O_2, dilution in N_2, τ=120 ms).

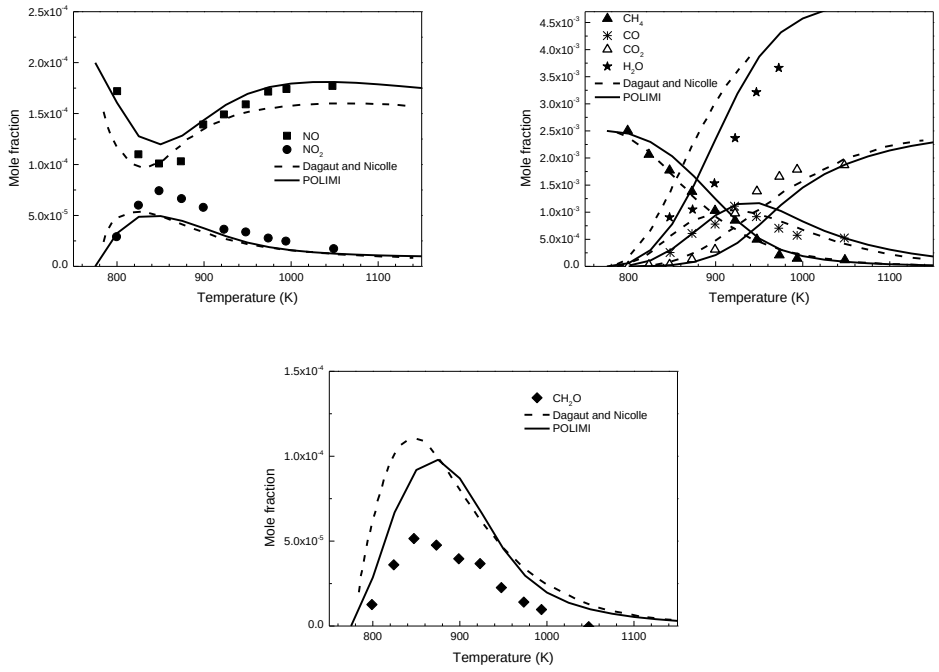

Fig.S3. Comparison of modeling predictions using POLIMI mechanism (solid lines) and experimental (symbols) and modeling predictions (dashed lines) reported by Dagaut and Nicolle [1] for the oxidation of methane and NO in a JSR (10 atm, Φ=0.5, 2500 ppm of CH_4, 10000 ppm of O_2, dilution in N_2, τ=1000 ms).

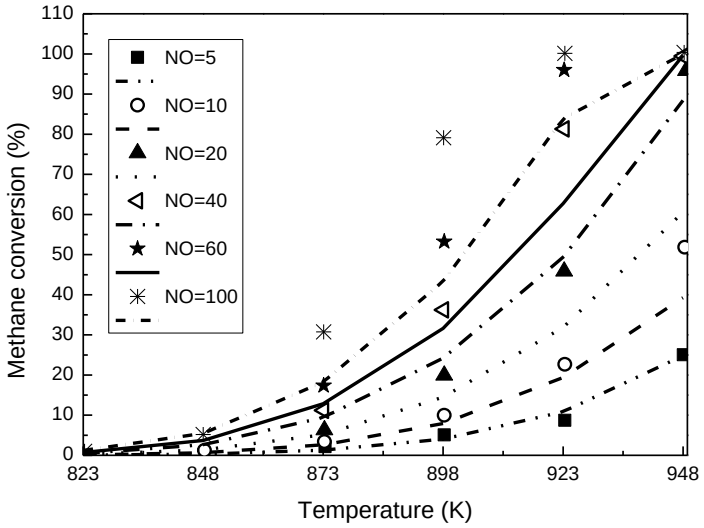

Fig.S4. Comparison of modeling predictions using POLIMI mechanism (lines) and experimental (symbols) reported by Chan et al. [2] for the oxidation of methane and different amounts of NO in a flow reactor (1 atm, 2.5% methane-in-air mixture, 0-100 ppm NO added, residence time of 2 s).

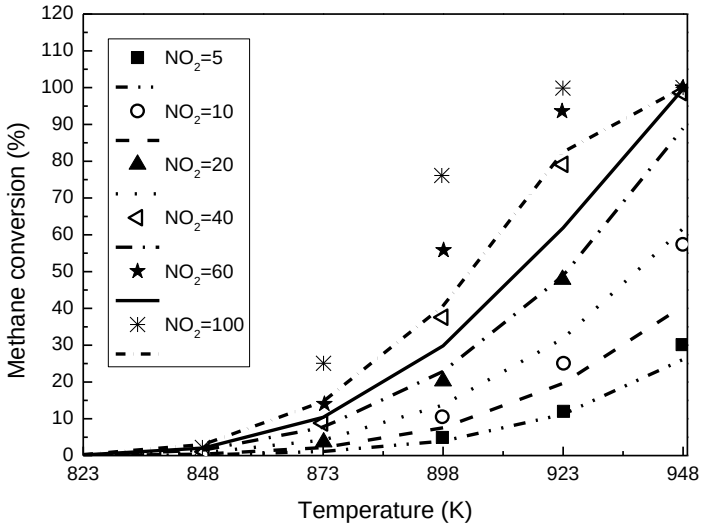

Fig.S5. Comparison of modeling predictions using POLIMI mechanism (lines) and experimental (symbols) reported by Chan et al. [2] for the oxidation of methane and different amounts of NO_2 in a flow reactor (1 atm, 2.5% methane-in-air mixture, 0-100 ppm NO_2 added, residence time of 2 s).

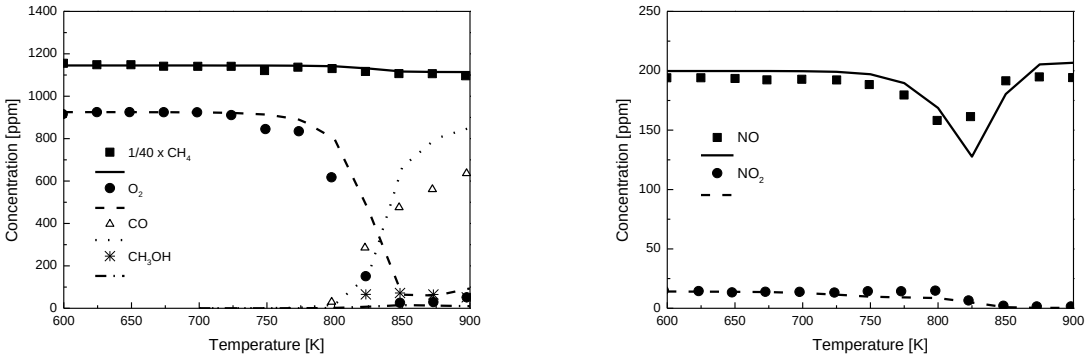

Fig.S6. Comparison of modeling predictions using POLIMI mechanism (lines) and experimental (symbols) reported by Rasmussen et al. [3] for the oxidation of methane and NO in a high-pressure flow reactor (20 bar, 4.58% methane, 925 ppm O_2, 200 ppm NO, 14 ppm NO_2, Φ=99, τ=2440/T).

3) The evolution profiles of methane as a function of time at both steady and oscillation states

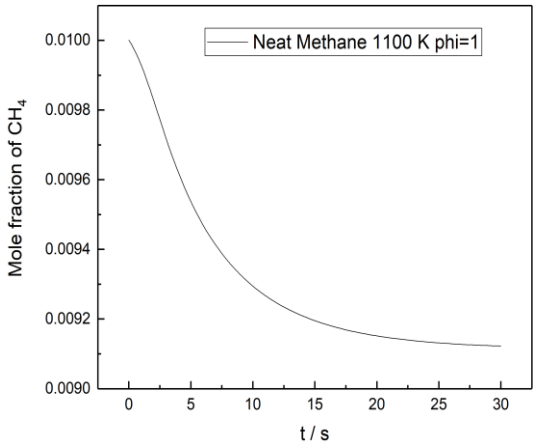

Fig.S7. The simulation work of the evolution profiles of methane as a function of time for the neat methane oxidation at 1100 K under stoichiometric condition. **(Steady state)**

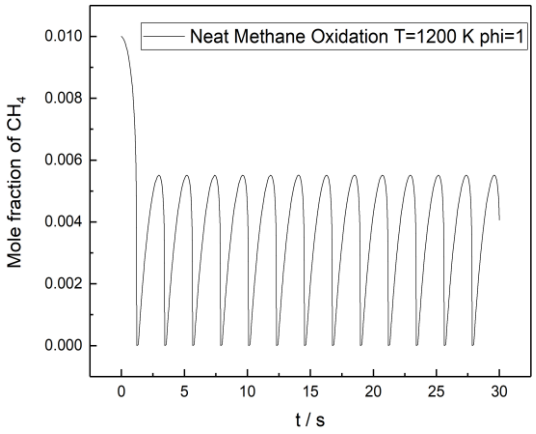

Fig.S8. The simulation work of the evolution profiles of methane as a function of time for the neat methane oxidation at 1200 K under stoichiometric condition. **(Oscillations)**

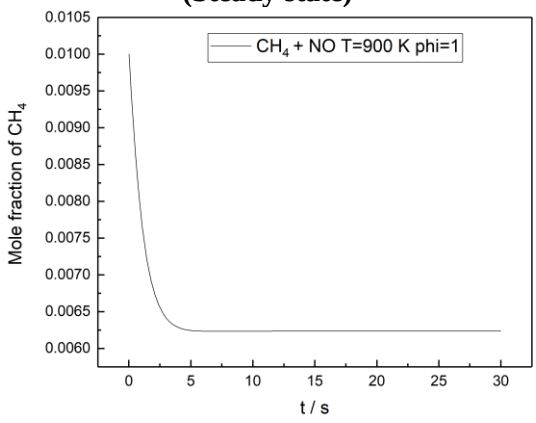

Fig.S9. The simulation work of the evolution profiles of methane as a function of time for the oxidation of methane doped with NO at 900 K under stoichiometric condition. **(Steady state)**

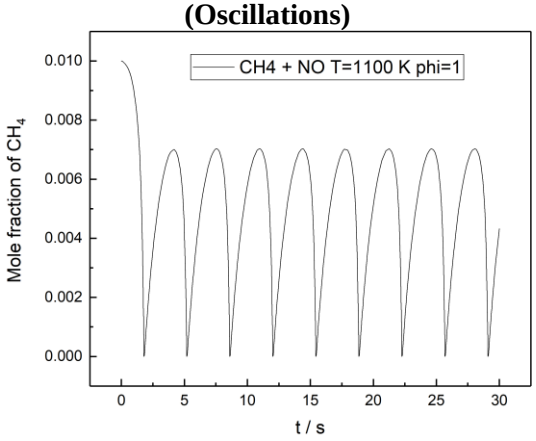

Fig.S10. The simulation work of the evolution profiles of methane as a function of time for the oxidation of methane doped with NO at 1000 K under stoichiometric condition. **(Oscillations)**

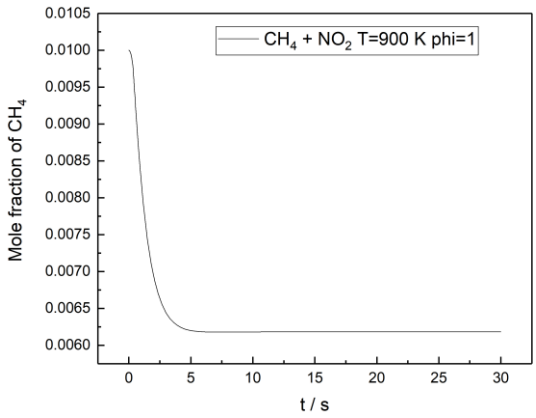

Fig.S11. The simulation work of the evolution profiles of methane as a function of time for the oxidation of methane doped with NO_2 at 900 K under stoichiometric condition. **(Steady state)**

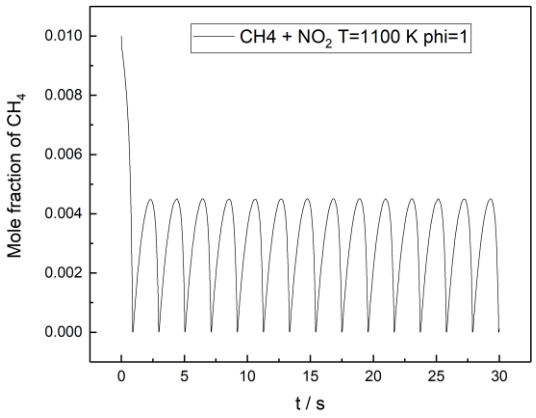

Fig.S12. The simulation work of the evolution profiles of methane as a function of time for the oxidation of methane doped with NO_2 at 1100 K under stoichiometric condition. **(Oscillations)**

4) Evolution with temperature of mole fractions of the different species according to model calculations with POLIMI mechanism.

A) For the addition of 400 ppm of NO_2 and Φ=2.

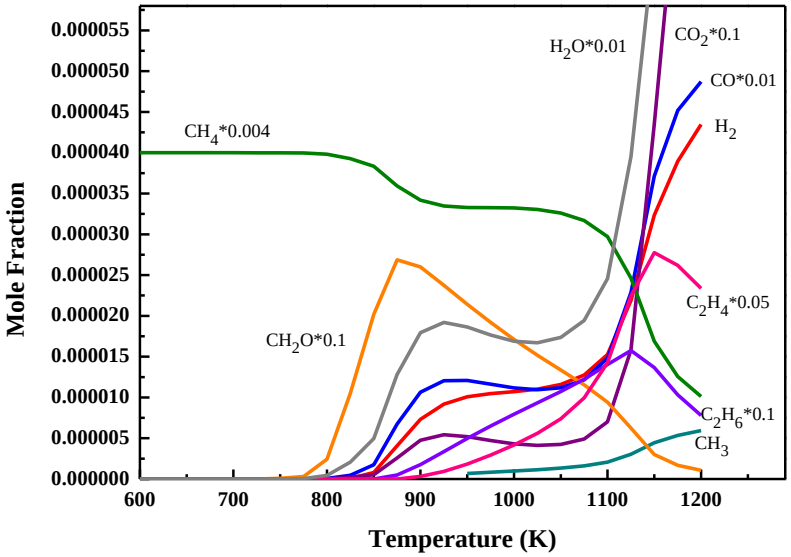

Fig.S13. Evolution with temperature of mole fractions for the carbon compound species, H_2O and H_2 predicted by the POLIMI mechanism for the addition of 400 ppm of NO_2 and Φ=2.

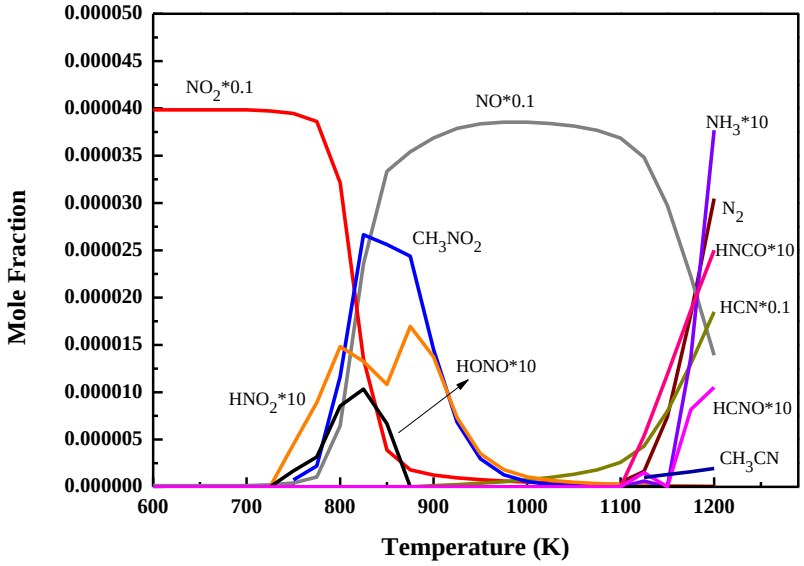

Fig.S14. Evolution with temperature of mole fractions for the nitrogen containing species predicted by the POLIMI mechanism for the addition of 400 ppm of NO_2 and Φ=2.

B) For the addition of 400 ppm of NO_2 and Φ=0.5

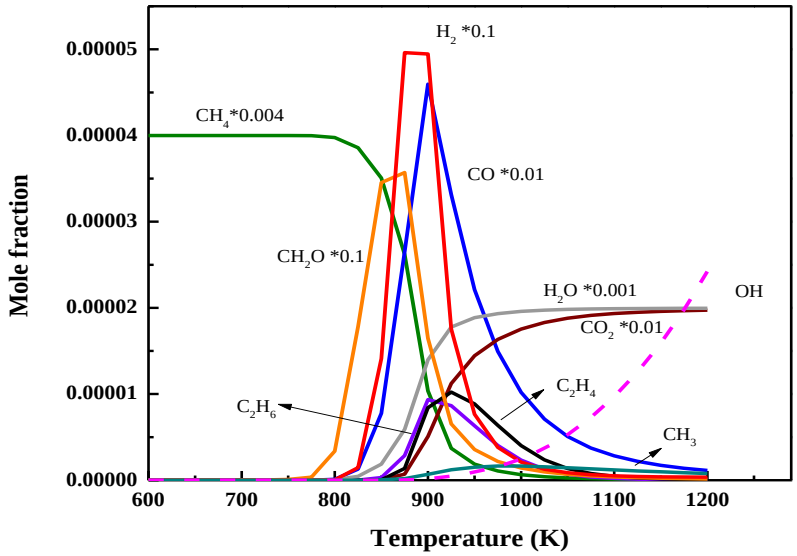

Fig.S15. Evolution with temperature of mole fractions for the carbon compound species, H_2O and H_2 predicted by the POLIMI mechanism for the addition of 400 ppm of NO_2 and Φ=0.5.

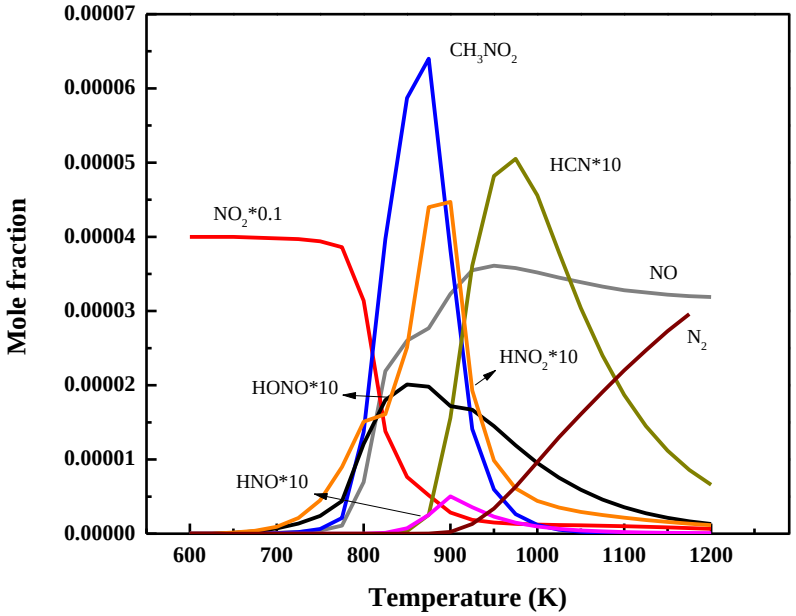

Fig.S16. Evolution with temperature of mole fractions for the nitrogen containing species predicted by the POLIMI mechanism for the addition of 400 ppm of NO_2 and Φ=0.5.

C) For the addition of 500 ppm of NO and Φ=2.

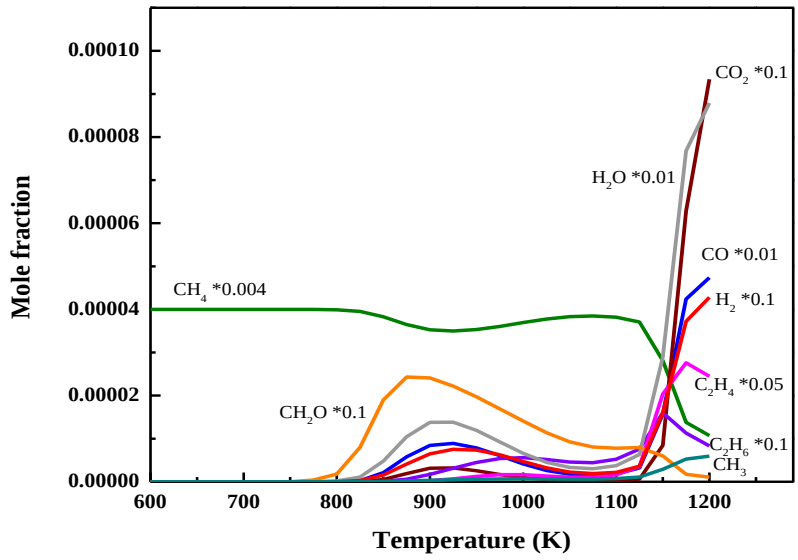

Fig.S17. Evolution with temperature of mole fractions for the carbon compound species, H_2O and H_2 predicted by the POLIMI mechanism for the addition of 500 ppm of NO and Φ=2.

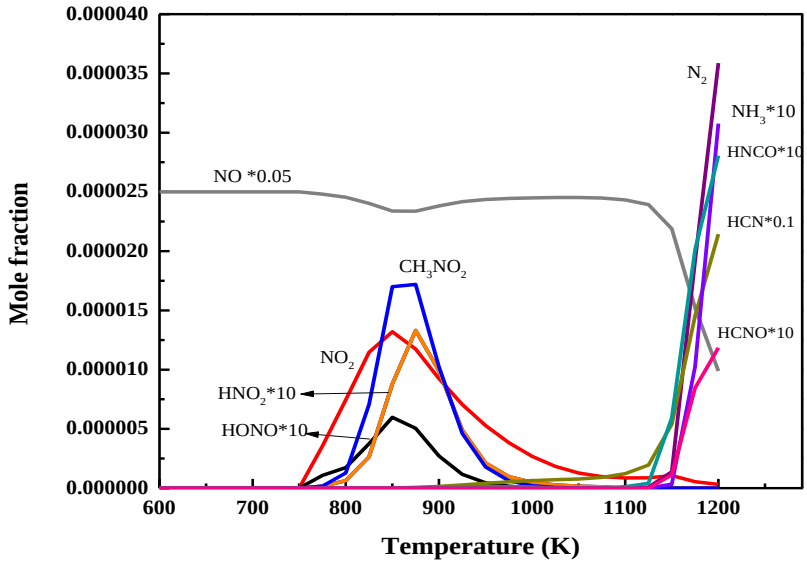

Fig.S18. Evolution with temperature of mole fractions for the nitrogen containing species predicted by the POLIMI mechanism for the addition of 500 ppm of NO and Φ=2.

D) For the addition of 500 ppm of NO and Φ=0.5.

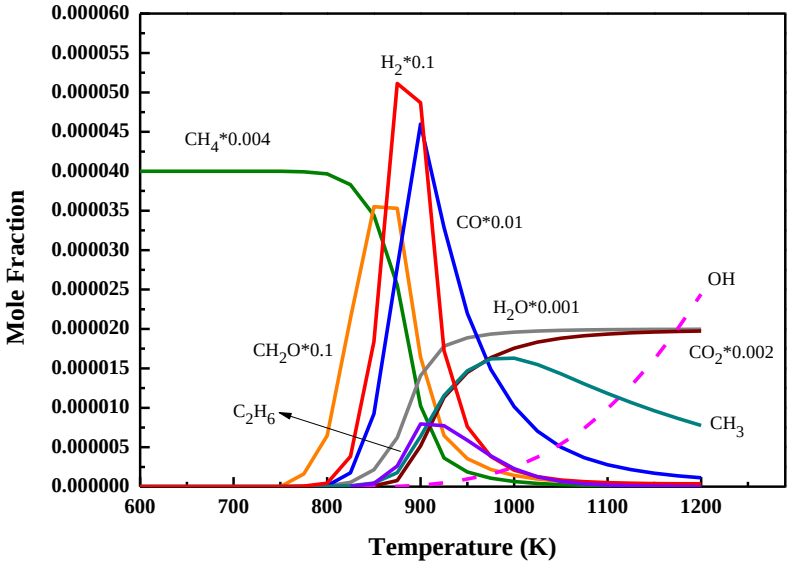

Fig.S19. Evolution with temperature of mole fractions for the carbon compound species, H_2O, H_2 and OH radicals predicted by the POLIMI mechanism for the addition of 500 ppm of NO and Φ=0.5.

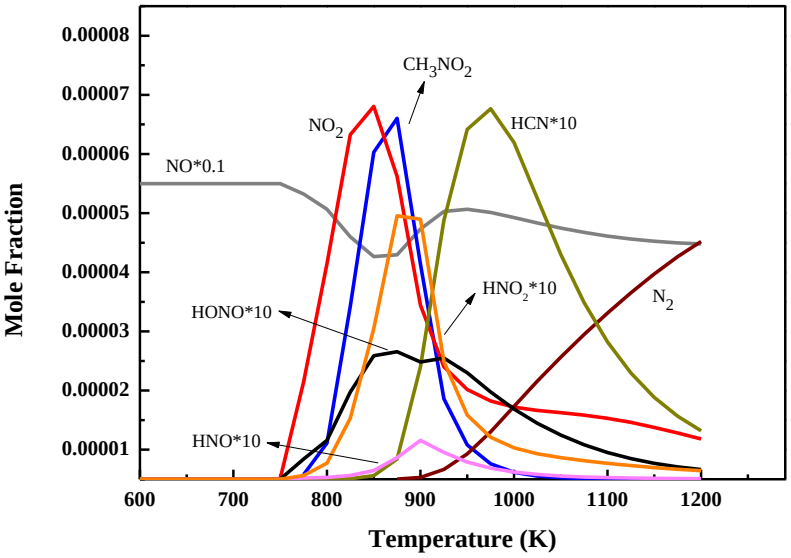

Fig.S20. Evolution with temperature of mole fractions for the nitrogen containing species predicted by the POLIMI mechanism for the addition of 500 ppm of NO and Φ=0.5.

5) The performance of literature models against the experimental data

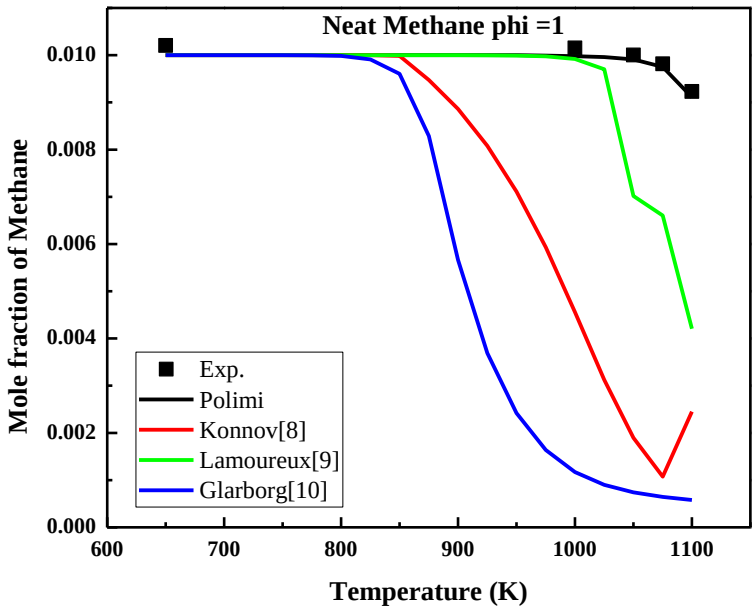

Fig.S21. The performance of different models against the experiment data (mole fraction of methane) with neat methane oxidation under stoichiometric conditions.

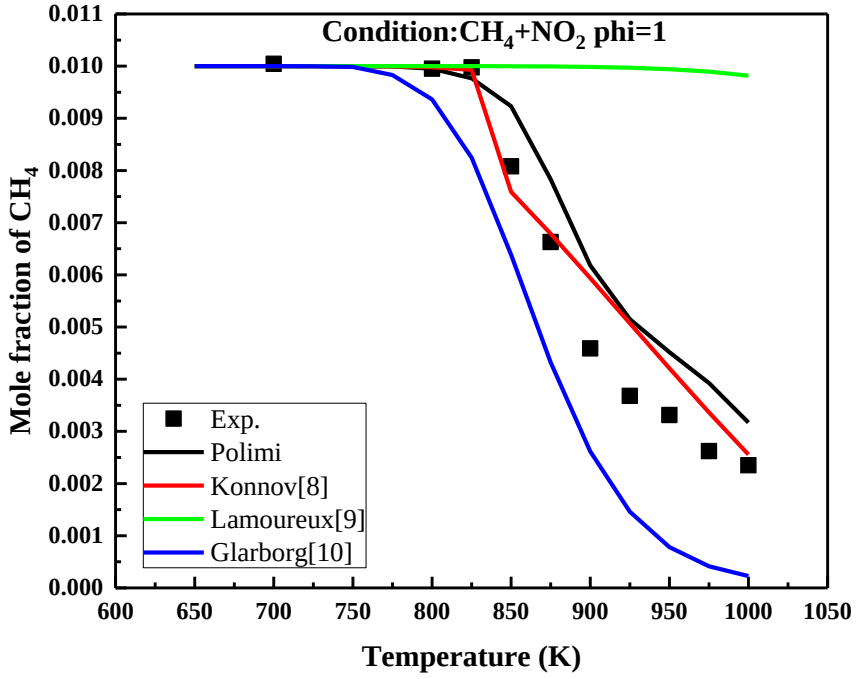

Fig.S22. The performance of different models against the experiment data (mole fraction of methane) with the oxidation of methane doped with NO_2 under stoichiometric conditions.

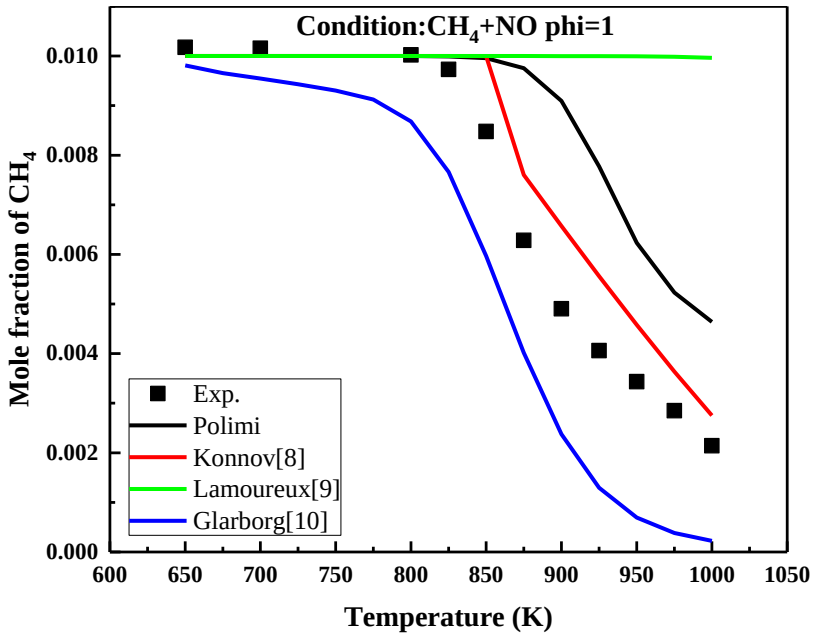

Fig.S23. The performance of different models against the experiment data (mole fraction of methane) with the oxidation of methane doped with NO under stoichiometric conditions.

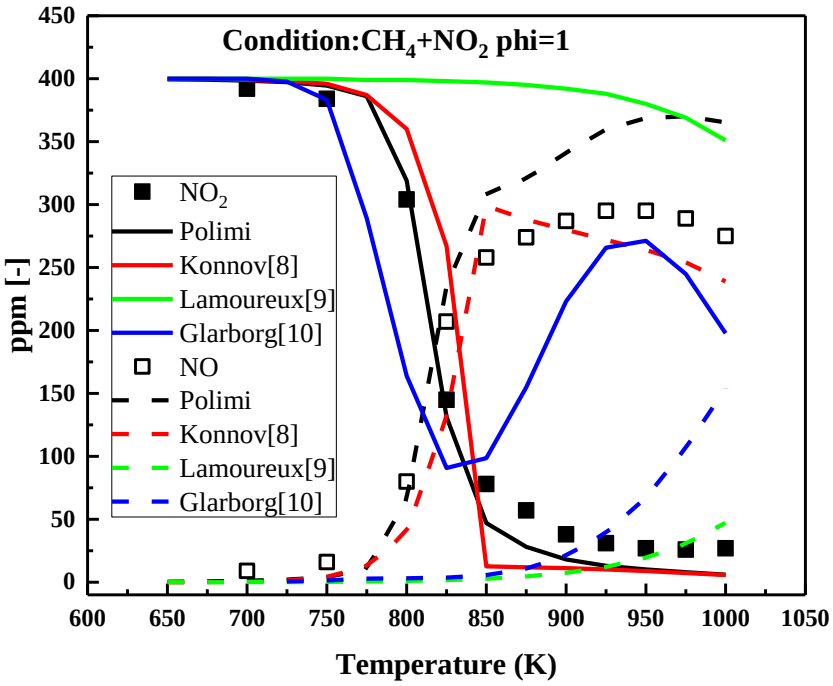

Fig.S24. The performance of different models against the experiment data (mole fraction of NO_x) with the oxidation of methane doped with NO_2 under stoichiometric conditions.

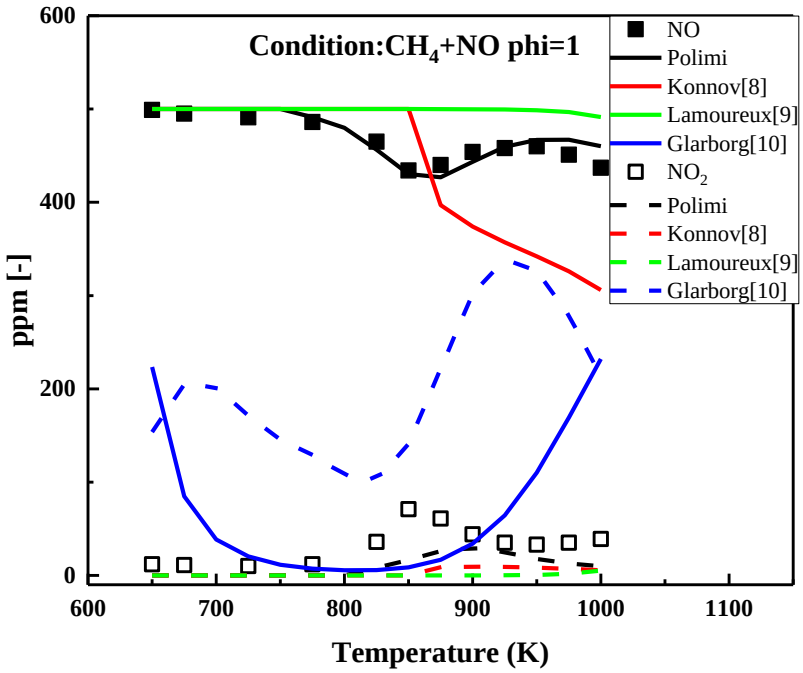

Fig.S25. The performance of different models against the experiment data (mole fraction of NO_x) with the oxidation of methane doped with NO under stoichiometric conditions.

6) Comparison of FTIR spectra for HCN with the spectra obtained during the oxidation of methane doped with NO.

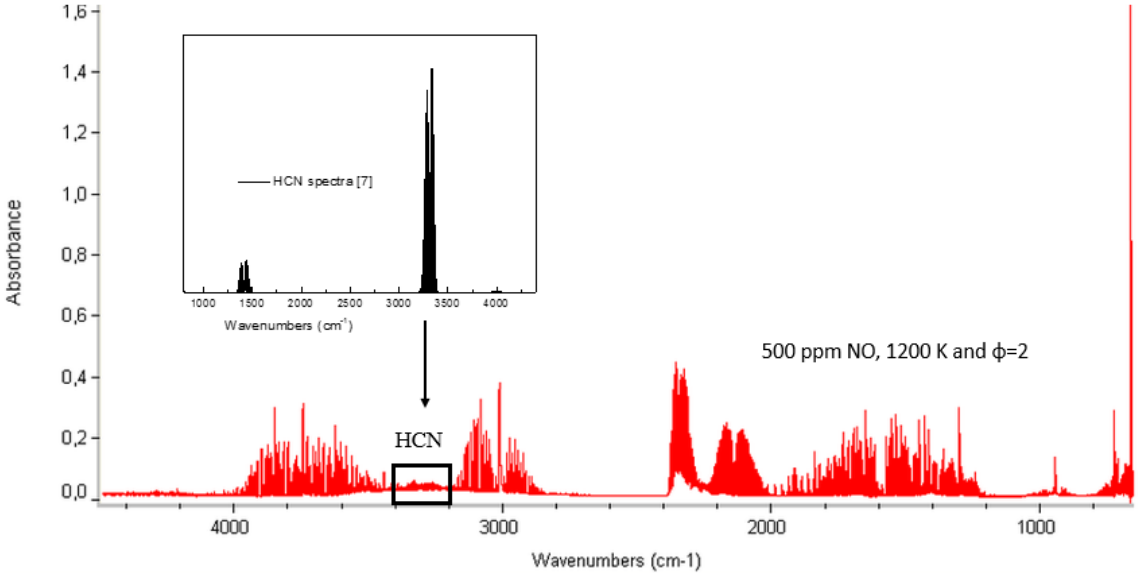

Fig.S26. Comparison of the FTIR spectra for HCN [7] with the spectra obtained during the oxidation of methane doped with NO (500 ppm NO, 1200 K and Φ=2).

7) Comparison of FTIR spectra for CH_3NO_2 with the spectra obtained during the oxidation of methane doped with NO_2.

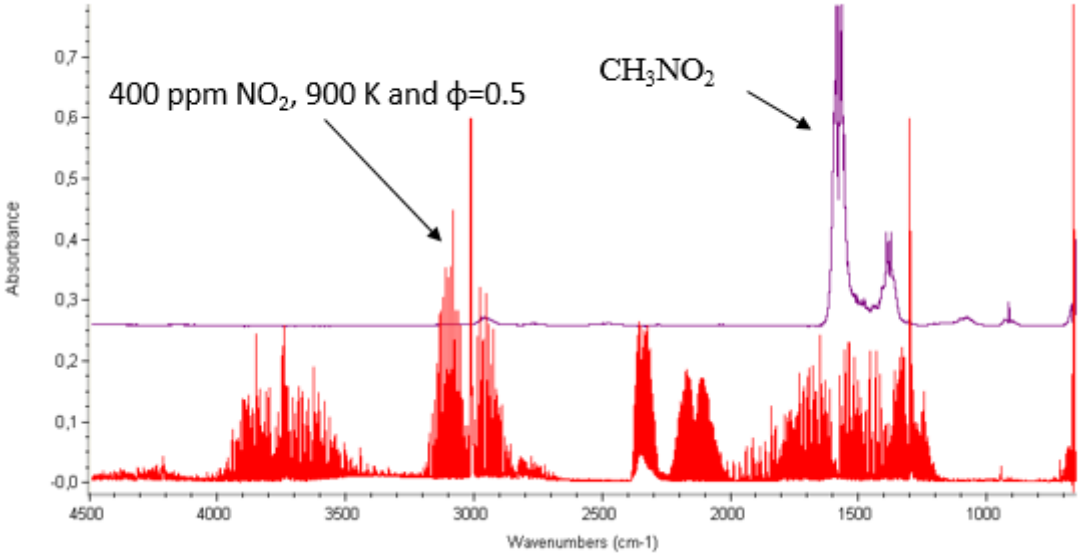

Fig.S27. Comparison of the FTIR spectra obtained for CH_3NO_2 with the spectra obtained during the oxidation of methane doped with NO_2 (400 ppm NO_2, 900 K and Φ=0.5).

8) Comparison of cw-CRDS spectra for HONO with the spectra obtained during the oxidation of methane doped with NO_2

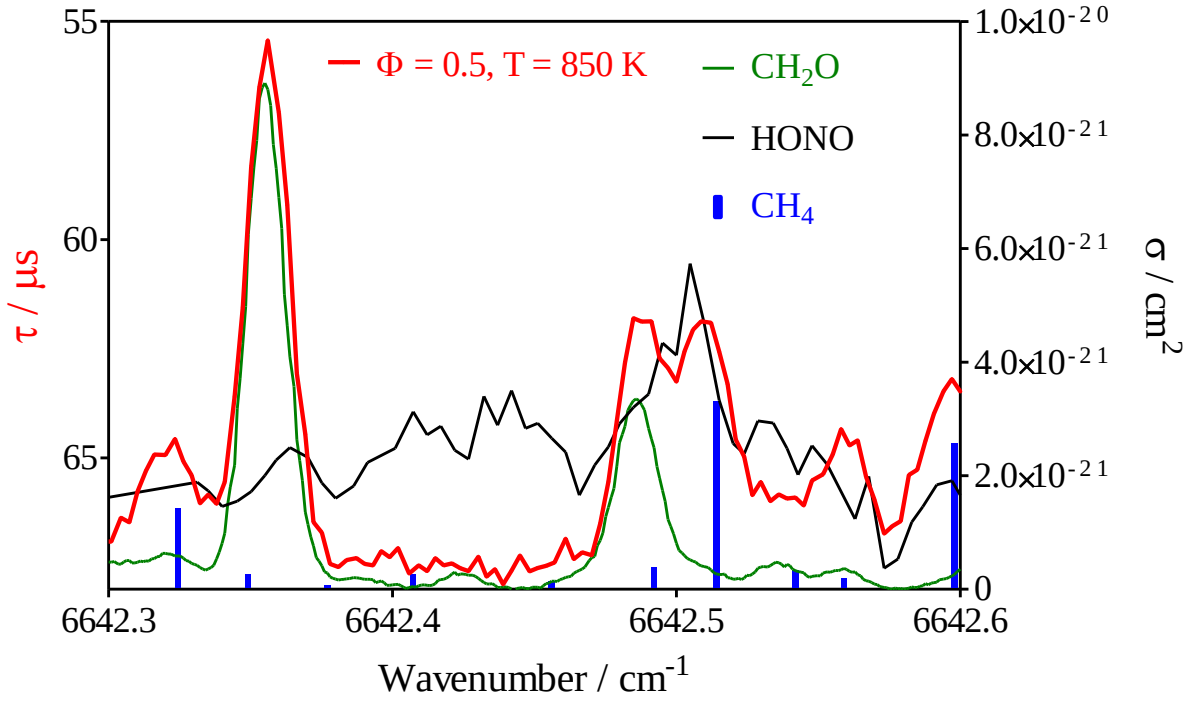

Fig.S28. Comparison of the HONO cw-CRDS spectra with the spectra obtained during the oxidation of CH_4 doped with 400 ppm NO_2, at 850 K and Φ=0.5. Red line: absorption spectrum measured in this work (left axis), black line: HONO spectrum from Jain et al. [4], green line: CH_2O absorption spectrum from Ruth et al. [5], multiplied by 12, blue bars: CH_4 line strengths from Liu et al. [6], multiplied by 10^4.

9) Comparisons between the original POLIMI model and POLIMI model with $CH_3+NO_2=CH_2O+NO$ modified against the experimental data under different conditions

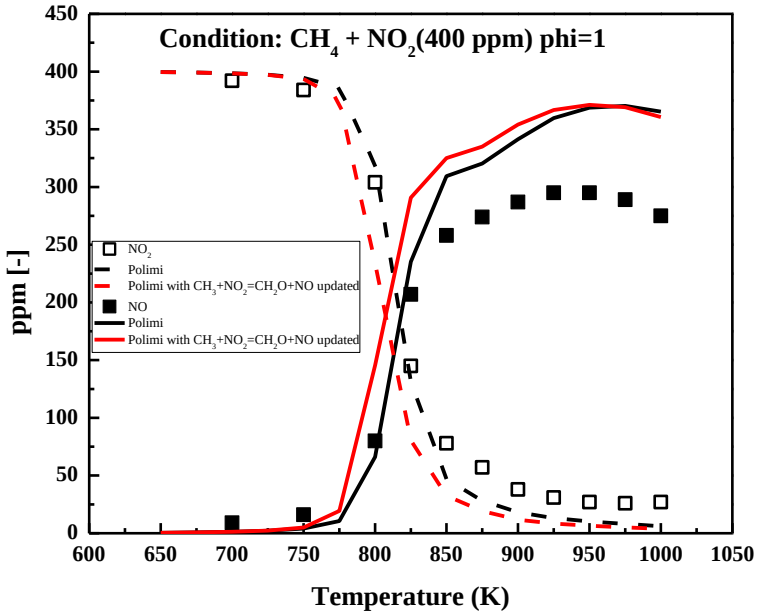

Fig.S29. Comparisons between the original POLIMI model and POLIMI model with $CH_3+NO_2=CH_2O+NO$ modified against the experimental results from the oxidation of methane doped with NO_2 under stoichiometric conditions.

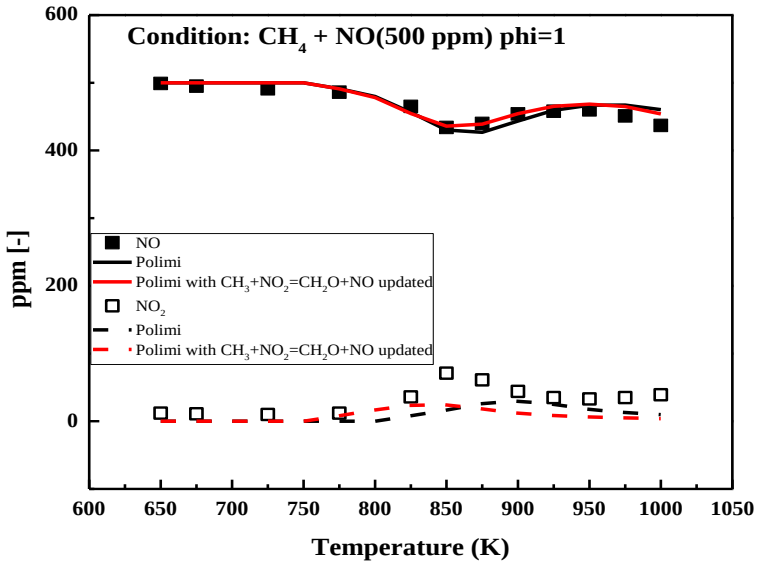

Fig.S30. Comparisons between the original POLIMI model and POLIMI model with $CH_3+NO_2=CH_2O+NO$ modified against the experimental results from the oxidation of methane doped with NO under stoichiometric conditions.

References

[1] P. Dagaut, A. Nicolle, *Combust. Flame* 140 (2005) 161-171.

[2] Y.L. Chan, F.J. Barnes, J.H. Bromly, A.A. Konnov, D.K. Zhang, *Proc. Combust. Inst.* 33 (2011) 441-447.

[3] C.L. Rasmussen, A.E. Rasmussen, P. Glarborg, *Combust. Flame* 154 (2008) 529-545.

[4] C. Jain, P. Morajkar, C. Schoemaecker, B. Viskolcz, C. Fittschen, *J. Phys. Chem. A* 115 (2011) 10720-10728.

[5] A.W. Liu, S. Kassi, A. Campargue, *Chem. Phys. Lett.* 447 (2007) 16-20.

[6] A.A. Ruth, U. Heitmann, E. Heinecke, C. Fittschen, *Z. Phys. Chem.* 229 (2015) 1609.

[7] The HITRAN Database, Website: http://hitran.org/

[8] A.A. Konnov, Combustion and Flame, 156 (2009) 2093-2105.

[9] N. Lamoureux, H. El Merhubi, L. Pillier, S. de Persis, P. Desgroux, Combustion and Flame, 163 (2016) 557-575.

[10] T. Mendiara, P. Glarborg, Combustion and Flame, 156 (2009) 1937-1949.